



Properties and environmental sustainability of fungal chitin nanofibril reinforced cellulose acetate films and nanofiber mats by solution blow spinning

Ana Kramar^{a,*}, Javier González-Benito^{a,b}, Nataša Nikolić^a, Aitor Larrañaga^c, Erlantz Lizundia^{d,e,**}

^a Department of Materials Science and Engineering and Chemical Engineering, Universidad Carlos III de Madrid, Avda. Universidad 30, 28911 Leganés, Spain

^b Instituto Tecnológico de Química y Materiales "Álvaro Alonso Barba", Universidad Carlos III de Madrid, Avda. Universidad 30, 28911 Leganés, Spain

^c Group of Science and Engineering of Polymeric Biomaterials (ZIBIO Group), Department of Mining, Metallurgy Engineering and Materials Science, POLYMAT, University of the Basque Country (UPV/EHU), Plaza Ingeniero Torres Quevedo 1, 48013 Bilbao, Biscay, Spain

^d Life Cycle Thinking Group, Department of Graphic Design and Engineering Projects, University of the Basque Country (UPV/EHU), Plaza Ingeniero Torres Quevedo 1, 48013 Bilbao, Biscay, Spain

^e BCMaterials, Basque Center for Materials, Applications and Nanostructures, Edif. Martina Casiano, Pl. 3 Parque Científico UPV/EHU Barrio Sarriena, 48940 Leioa, Biscay, Spain

ARTICLE INFO

Keywords:

Chitin nanofibrils
Solution blow spinning
Life cycle assessment

ABSTRACT

Materials from biological origin composed by renewable carbon facilitate the transition from linear carbon-intensive economy to a sustainable circular economy. Accordingly, we use solution blow spinning to develop fully biobased cellulose acetate films and nanofiber mats reinforced with fungal chitin nanofibrils (ChNFs), an emerging bio-colloid with lower carbon footprint compared to crustacean-derived nanochitin. This study incorporates fungal ChNFs into spinning processes for the first time. ChNF addition reduces film surface roughness, modifies film water affinity, and tailors the nanofiber diameter of the mats. The covalently bonded β -D-glucans of ChNFs act as a binder to improve the interfacial properties and consequently load transference to enhance the mechanical properties. Accordingly, the Young's modulus of the films increases from 200 ± 18 MPa to 359 ± 99 MPa with 1.5 wt% ChNFs, while the elongation at break increases by ~ 45 %. Life cycle assessment (LCA) is applied to quantify the environmental impacts of solution blow spinning for the first time, providing global warming potential values of 69.7–347.4 kg-CO₂-equiv·kg⁻¹. Additionally, this work highlights the suitability of ChNFs as reinforcing fillers during spinning and proves the reinforcing effect of mushroom-derived chitin in biobased films, opening alternatives for sustainable materials development beyond nanocelluloses in the near future.

1. Introduction

Driven by the scarcity of raw materials, declining availability of fossil resources, and the climate crisis, there is an urgent need to transition from a linear economy, based on fossil-derived materials, to a sustainable circular economy based on renewable materials [1,2]. Materials of biological origin are generally abundant, non-toxic, and biodegradable [3]. Importantly, renewable feedstocks offer the additional

environmental advantage of being composed by renewable carbon, so their utilization does not incorporate fossil carbon from the ground into the carbon cycle above the ground. As such, materials containing renewable carbon have the potential to mitigate climate change by reducing greenhouse gases over their conventional petroleum-derived counterparts. Cellulose, as the most common bio-based polymer on the Earth, and its derivatives are popular materials for packaging, food industry, paper industry, or construction applications. Cellulose acetate

* Correspondence to: A. Kramar, Novel Materials and Nanotechnology Group, Institute of Agrochemistry and Food Technology (IATA) Spanish Council for Scientific Research (CSIC), Calle Catedrático Agustín Escardino Benlloch 7, 46980 Paterna, Spain.

** Correspondence to: E. Lizundia, Life Cycle Thinking Group, Department of Graphic Design and Engineering Projects, University of the Basque Country (UPV/EHU), Plaza Ingeniero Torres Quevedo 1, 48013 Bilbao, Biscay, Spain.

E-mail addresses: akramar@iata.csic.es (A. Kramar), erlantz.liizundia@ehu.eus (E. Lizundia).

<https://doi.org/10.1016/j.ijbiomac.2024.132046>

Received 18 September 2023; Received in revised form 26 April 2024; Accepted 30 April 2024

Available online 7 May 2024

0141-8130/© 2024 The Authors. Published by Elsevier B.V. This is an open access article under the CC BY license (<http://creativecommons.org/licenses/by/4.0/>).

(CA) is a widely used cellulose ester due to its mechanical toughness and flexibility in the form of films or fibers, as well as adequate processability. CA is partially acetylated cellulose that can be obtained from non-edible plants using acetic acid, the main constituent of vinegar. CA films have multiple applications, including environmental remediation [4], active packaging [5], and gas barrier [6]. Besides, CA electrospun nanofiber mats can be used even for tissue engineering/textiles [7].

To expand its applications, CA can be reinforced with nanoparticles. The majority of nanofillers used in this context are metallic nanoparticles or graphene, as in the case of electrospun CA [8–11] or cellulose regenerated from electrospun CA [12]. The CA electrospun mats reinforced with nanoparticles can be used in biomedicine [8,11,13,14] or for environmental purposes as efficient adsorbents of pollutants [9,15]. When exploring alternatives to metallic and graphene-based nanofillers, bio-based colloids are a promising environmental and economical option due to their often self-excluding characteristics of renewability, competitive thermo-mechanical behavior and biodegradability [16,17]. The mechanical, optical, thermal, and ionic properties of bio-colloids are above the properties shown by their corresponding parent material [17]. In recent years, nanocelluloses such as cellulose nanocrystals (CNCs), or cellulose nanofibers (CNFs), have gained significant attention from both academia and industry. They are now used in areas as varied as packaging [18], construction [19], food industry [20], additive manufacturing [21], sustainable electronics [22], or drug delivery [23]. Nanocelluloses are isolated from native cellulose using a top-down approach that involves a controlled mechanical or chemical deconstruction process [17]. Currently, several companies commercializing CNCs and CNFs can be found [17,24,25], indicating a notable increase in the technology readiness level.

Given the extensive range of natural macromolecules, numerous materials can be potentially nanofibrillated to obtain bio-based colloids, resulting in materials with multiple functions. With a relatively similar chemical structure to cellulose, chitin can also be deconstructed to produce chitin nanocrystals (ChNCs) [26]. Thanks to its acetamide groups, nanochitin offers certain advantages over its nanocellulose analogue for applications in photonic devices [27], energy storage [28], or barrier applications in films [29]. Conventional ChNC isolation usually requires harsh chemical and/or mechanical treatments, such as strong acid hydrolysis (1–4 M HCl) and/or chemical oxidation steps to demineralize the arthropod exoskeletons and remove the CaCO_3 . Then, the remaining material undergoes through a deproteinization process using NaOH material. Finally, the resulting chitin can be bleached and fibrillated to obtain ChNCs [16]. However, these methods result in significant wastewater generation (acidic and alkali from demineralization and deproteinization, respectively) and a notable CO_2 footprint, jeopardizing its implementation in the industrial processing of sustainable materials. The transition towards bio-based sustainable materials requires new methods of nanochitin isolation.

Chitin is a primary component of cell walls in fungi, including filamentous and mushroom-forming fungi [30]. Interestingly, fungal chitin does not coexist with CaCO_3 , which suggests the possibility of avoiding the use of strong acid hydrolysis required to demineralize crustacean shells. Consequently, chitin nanofibrils (ChNFs) can be isolated under mild conditions utilizing NaOH to obtain a global warming potential of $18.5 \text{ kg CO}_2\text{-equiv}\cdot\text{kg}^{-1}$ [31]. Although wastewater is still generated from the deproteinization process in ChNFs (alkali treatment), significantly lower carbon footprint values than the $543.5\text{--}906.8 \text{ kg CO}_2\text{-equiv}\cdot\text{kg}^{-1}$ generated upon ChNC isolation from crab or shrimp shells can be obtained [31]. For the purposes of comparison, petroleum-derived polymers with optimized supply chain and production processes have global warming potential values of $2.0 \text{ kg CO}_2\text{-equiv}\cdot\text{kg}^{-1}$ for polypropylene and polyethylene, $3.8 \text{ kg CO}_2\text{-equiv}\cdot\text{kg}^{-1}$ for polystyrene, $5.3 \text{ kg CO}_2\text{-equiv}\cdot\text{kg}^{-1}$ for polycarbonate, or $16.6 \text{ kg CO}_2\text{-equiv}\cdot\text{kg}^{-1}$ for polyvinylfluoride (according to ecoinvent v3.9.1 database). These data clearly demonstrate the potential of ChNF to provide sustainable bioproducts once production processes are optimized and

scaled up. A particularly interesting aspect of fungal ChNFs is the presence of covalently linked β -D-glucans, polysaccharides having D-glucose monomers and β -glycosidic bonds. These glucans offer notable advantages in terms of mechanical reinforcement [32], environmental remediation [33], and transient zinc-ion batteries that degrade upon immersion in water [34]. However, there are relatively few reports on ChNFs compared to its analogous cellulosic counterparts, suggesting that its full potential has yet to be explored.

For the preparation of CA materials, traditional solution casting and electrospinning are commonly utilized techniques [35]. Solution casting is a simple method for obtaining free-standing non-porous films, while electrospinning produces complex morphologies and fibrous membranes that can expand the application range of CA into areas such as filtration membranes [36], or wound dressings [37]. However, electrospinning requires a high electric field, which limits up-scaling possibilities due to relatively low production rates. In contrast, solution blow spinning (SBS), first introduced in 2009, may be a faster fabrication procedure that can also produce tailored fibrous morphologies like electrospinning [38,39]. In addition to selecting adequate processing conditions, SBS can be utilized to produce nano/submicrometric fibers and prepare materials that exhibit morphological features of both films and fibers [38,40–42]. During SBS processing, a polymeric solution is pumped through the inner channel of a nozzle while high-velocity pressurized air at 0.5–4 bar flows along the outer channel of the nozzle. This causes the air to exert a force on the polymer solution at the exit of the nozzle, creating a jet and accelerating solvent elimination by evaporation. Finally, the jet turns into a solid polymer that can be in the form of thin fibers. Since the production of the materials is not limited to a grounded collector, SBS can be directly applied to targeted surfaces such as skin [43], or historical bones [44]. Another significant advantage of SBS is its ability to achieve uniform nanoparticle dispersions within polymer matrices during production [41,45].

The current work incorporates fungal ChNFs into a polymer matrix for the first time using a spinning technique. Additionally, fungal ChNFs are incorporated in both films and nanofibrous mats using the same technique while changing only the composition of the solution. Most importantly, the results obtained here provide new insights for future design of parameters in conventional and non-conventional fiber spinning techniques, including wet spinning, dry spinning, melt spinning, electrospinning, and ultimately solution blow spinning. Finally, the environmental impacts originated from solution blow spinning are quantified for the first time using the well-recognized life cycle assessment (LCA) methodology. Obtained carbon footprint, water consumption, acidification and eutrophication impacts provide novel information for the development of more sustainable processes in the near future. CA was chosen as a representative matrix due to its versatility for production similarly to common synthetic plastics, while preserving its natural origin and biodegradation. Nanocomposites of CA films and CA/PEO/ChNFs nanofibrous mats, containing up to 5 wt% of ChNFs were investigated in terms of processing, structure, thermal properties, and morphology. ChNFs exhibit a significant mechanical reinforcing effect in CA films due to their nanofibrous morphology and the presence of glucans, which provide a natural composite structure [32]. When processed as nanofibrous composites, ChNFs improve the toughness of the resulting materials and prevents sudden failure of the material when tensile stress is applied. This work utilizes materials having renewable carbon to demonstrate that ChNFs derived from fungi can serve as reinforcing nanofillers in bio-based polymers, providing further alternatives for sustainable material development beyond nanocelluloses.

2. Materials and methods

2.1. Materials

White mushrooms, *Agaricus bisporus*, were obtained from a local

store in Bilbao, Spain. Cellulose acetate (CA) with a M_n of 30.000 $\text{g}\cdot\text{mol}^{-1}$ and a degree of substitution (DS) of 2.45 (determined by saponification method according to standard ASTM D871–96), poly (ethylene oxide) powder (PEO) (M_v of 100.000 $\text{g}\cdot\text{mol}^{-1}$), acetone (Ac) (HPLC >99.9 %), sodium hydroxide (NaOH) pellets (99 %), chloroform (anhydrous, ≥ 99 %) and N,N-dimethylformamide (DMF) (HPLC >99.9 %) were supplied by Sigma Merck and used as received without further purification.

2.2. Chitin nanofibril isolation

To isolate colloidal ChNFs from the whole fruiting body of *Agaricus bisporus*, a top-down approach was used to selectively remove the proteins in fungi [32,34]. Firstly, the fresh mushrooms were frozen at -12 °C for seven days to prevent unwanted enzymatic degradation events. To isolate ChNFs, 300 g of frozen *Agaricus bisporus* was thawed in 600 mL of distilled water for 15 min and then washed to remove the soil and other impurities. The washed mushrooms were mechanically blended for 5 min using a kitchen blender (Stabmixer KOENIG). The slurry was heated at 85 °C for 30 min under magnetic stirring to remove the water-soluble components. After washing by centrifugation at 4000 rpm for 15 min, the remaining material was treated using a 1 M NaOH at 65 °C for 180 min under magnetic stirring. This step removes proteins, lipids, and alkaline-soluble polysaccharides. After washing and centrifuging at 4000 rpm for 15 min, the remaining material was re-suspended in water at a concentration of 2 wt% and blended for 5 min. The dispersion was stored in a refrigerator at 4 °C until use. The ChNFs exhibited diameters of approximately 80 nm and lengths extending up to few micrometers [34].

2.3. Solution preparation for films

The solutions were prepared by dissolving CA in a mixture of solvents, specifically acetone and DMF in 7:3 ratio v/v. This was done 24 h prior to processing, resulting in a final volume of 10 mL and CA concentration of 12 % (w/v). Before solution blow spinning, the ChNFs were solvent-exchanged in acetone. To do this, the required amount of water suspension was placed into a centrifuge tube and double volume of acetone was added. The suspension underwent sonication for 10 min using an Ultrasonic bath ATU ATM series, followed by centrifugation for 15 min at 9000 rpm in a Centrifuge Orto Alresa digicen 21 with fixed rotor RT 154. The excess liquid was removed and further fresh acetone was added. The solution was sonicated for 10 min with additional 15 s of ultrasound probe (SONIX Vibra-cell 750 W, 20 kHz), followed by another centrifugation at 9000 rpm for 15 min. The excess of liquid was removed and ChNFs suspension in acetone was added to the CA solution in acetone/DMF (Fig. 1). The final solution was sonicated for 15 s with a

US probe, then treated in an ultrasonication bath for 10 min and finally stirred for 30 min using a magnetic stirrer. The resulting material was inserted into a syringe and processed with the solution blow spinning machine.

2.4. Solution fabrication for polymer composite nanofibers

For solution blow spinning, individual solutions of CA and PEO were prepared 24 h in advance [46]. CA (10 w/v %) was dissolved in pure acetone under magnetic stirring into a reduced volume. First, 10 w/v % PEO dissolved in acetone/chloroform 6:4 v/v was mixed and stirred with CA solution in 8:2 ratio. Finally, the dispersed ChNFs in acetone were added, making a total volume of 10 mL. Similarly to the films, the CA/PEO/ChNF mixture was sonicated for 15 s, then treated in an ultrasonication bath for 10 min. Finally, it was subjected to an additional homogenization by magnetic stirring for 30 min. The suspension was then transferred to a syringe. Solvent exchange for ChNFs was always performed immediately before spinning and adding them to CA solutions to prevent their undesired aggregation in acetone and avoid acetone evaporation.

2.5. Solution blow spinning

The solution blow spinning apparatus was designed and manufactured in the Department of Materials Science and Engineering at UC3M [38,42,45–49]. The device comprises of a 3D printed nozzle connected to a high-pressure air supplier, a cylindrical collector rotating at 50-to-250 rpm, and an injection pump with injection rates of 0.12-to-0.25 $\text{mL}\cdot\text{min}^{-1}$. The capillary diameter in the nozzle through which the suspensions are made to flow is 0.6 mm. The distance from the nozzle to the collector was set at 10 cm for film preparation and 15 cm for mat preparation. The collector speed was set at 250 rpm, and a 10 mL syringe volume was used. Feeding rates and air pressure were adjusted depending on the system being injected into the nozzle to ensure uninterrupted processing. The sample code can be found in Table 1.

2.6. Morphology, structure and physico-chemical characterization

Room temperature X-ray diffraction (XRD) was conducted in a PHILIPS X'PERT PRO automatic diffractometer in theta–theta configuration, secondary monochromator with Cu-K α radiation ($\lambda = 1.5418$ Å) and a PIXcel solid state detector (active length in 2θ 3.347°). Data were collected from 5 to 50° 2θ (step size = 0.026) scan speed 0.0167° s^{-1} , at room temperature.

Attenuated total reflectance Fourier transform infrared (ATR-FTIR) spectra were acquired using a Thermo Fisher Nicolet iS5 spectrometer coupled with an ATR device with a diamond window GladiATR (PIKE Technologies). Measurements were performed in a range 500–3800

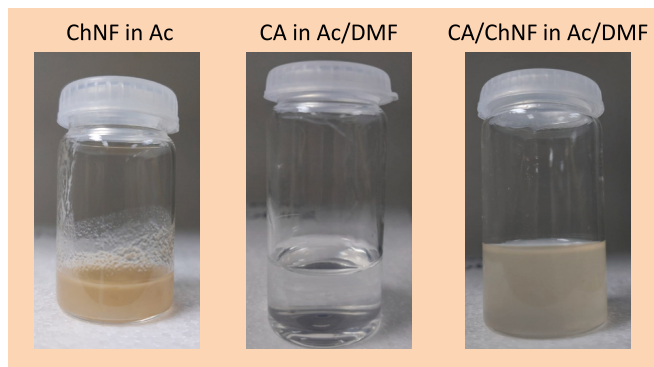


Fig. 1. Photographs of solutions used for preparation of the CA/ChNF mixtures to be processed by SBS; ChNF-chitin nanofibrils suspension in acetone, cellulose acetate CA dissolved in acetone/DMF mixture and final mixture of CA and ChNF.

Table 1
Sample codes and summary of solution blow spinning conditions to prepare the materials.

Sample code	Solution composition	Injection rate ($\text{mL}\cdot\text{min}^{-1}$)	Air pressure (bar)
CA-F	CA 12 % w/v, Ac/DMF 7:3	0.25	2.0
CA-F-ChNF 1	CA 12 % w/v, 1.5 wt% ChNF, Ac/DMF 7:3	0.25	1.6
CA-F-ChNF 2	CA 12 % w/v, 2.5 wt% ChNF, Ac/DMF 7:3	0.12	1.6
NF 0	CA/PEO (4:1) (1 g total in 10 mL solution)	0.25	1.6
NF-ChNF 1	CA/PEO (4:1) (10 % mix +1 wt% ChNF)	0.25	1.8
NF-ChNF 2	CA/PEO (4:1) (10 % mix +2 wt% ChNF)	0.25	1.6
NF-ChNF 3	CA/PEO (4:1) (10 % mix +5 wt% ChNF)	0.12	1.6

cm^{-1} using 32 scans and 4 cm^{-1} of resolution. Background recording was done before each sample recording.

Carbon nuclear magnetic resonance (^{13}C NMR) experiments were conducted using a Bruker Avance DPX 300 (Bruker, U.S.A.) at a resonance frequency of 75.5 MHz. The spectrum was obtained at room temperature using 40 mg, an inverse gated decoupled sequence, a 3 s acquisition time, a 4 s delay time, a $5.5 \mu\text{s}$ pulse, a spectral width of 18,800 Hz, and $> 10,000$ scans.

The morphology of the ChNFs was observed via transmission electron microscopy (TEM) using a JEOL JEM 1400 Plus apparatus with an acceleration voltage of 100 kV. A $3 \mu\text{L}$ droplet of a 0.05 wt% aqueous ChNF dispersion was deposited onto a hydrophilic EMS CF300-Cu grid treated by glow discharge treatment. Before observations, the material was stained using 1 % uranyl acetate for 20 s, after which the uranyl acetate was removed with a filter paper. The morphology of films and nanofiber mats was evaluated using a HitachiS-4800 field-emission scanning electron microscope (FE-SEM) at an acceleration voltage of 5 kV. Before imaging, samples were sputtered with a thin gold-palladium layer. Image analysis of nanofiber mats was performed using ImageJ software, and size distribution analysis was based on 150 measurements of each NF sample.

Optical microscope Olympus DSX500 (Olympus Iberia, Barcelona, Spain) was used to study roughness of films. R_a (arithmetic mean roughness) obtained from a sample area of $1994 \times 1994 \mu\text{m}$ was considered as the parameter to describe the roughness. The cut-off wavelength λ_c in the roughness analysis was chosen according to the standard EN ISO 4288-1997. The final value of R_a was obtained as the average of the results arising from 10 linear profiles (5 in the X direction and 5 in the Y direction). Both sides of the samples were considered, the upper one (in contact with air during SBS) and that one at the bottom (in contact with the collector).

Water contact angle was determined by depositing small drops of distilled and deionized water on the surfaces of the materials (on both sides for each sample) using a 23G needle. After that, photographs of the water drops were taken and angles were measured using plugin Drop Analysis - DropSnake [50] of the free software Fiji (ImageJ). Eight measurements were performed for each sample (four contact angle values on each side). Water contact angle measurements were performed only on film samples, since the nanofibrous materials contain water-soluble PEO and swell significantly, as shown in our previous work where we optimized procedure for preparation of composite CA/PEO nanofibers [46].

The thermodegradation of the samples (5–10 mg) was monitored with a TA Instruments TGA instrument (model Q50–0545) using platinum pans at a heating rate of $10 \text{ }^\circ\text{C}\cdot\text{min}^{-1}$ with a $60 \text{ mL}\cdot\text{min}^{-1}$ N_2 flow.

Mechanical behavior was studied using a Universal testing machine Microtest DT/005/FR (Microtest S.A., Madrid, Spain) with a load cell of 50 N. Specimens were tested in a uniaxial tensile configuration using a loading rate of $5 \text{ mm}\cdot\text{min}^{-1}$. The dimensions of the specimens were 40 mm length, 10 mm width (NF) or 5 mm (films), and the gap between the grips was 20 mm. Mechanical tests were done 5 times for each sample using specimens cut in the direction of the collector rotation during SBS. Specimen's thickness was measured before each test using Digimatic micrometer (Mitutoyo Corporation, Barcelona, Spain) of $\pm 1 \mu\text{m}$ accuracy.

2.7. Environmental impact assessment

The life cycle assessment (LCA) methodology has been used to quantify the environmental impacts of fabricated films and nanofiber mats. Our study considers the required raw materials, energy needs for *on-site* production by SBS, and waste treatment, including the wastewater generated during ChNF isolation. The electricity mix of the Spanish grid in November 2023 was used (full distribution is shown in Fig. S1), while the life cycle inventory is disclosed in Table S1 to facilitate comparison. Due to the lack of all utilized materials, certain

approximations have been considered. Briefly, cellulose acetate was replaced by carboxymethyl cellulose, while poly(ethylene oxide) was replaced by the average value from ethylene glycol and polyethylene production. The impacts corresponding to ChNFs were retrieved from a recent report [31]. The *cradle-to-gate* impacts have been determined according to the International Standards ISO 14040/14044 using OpenLCA 2.1.0 software, ecoinvent v3.9.1 database and the ReCiPe 2016 Midpoint (H) assessment methodology. The *global warming potential* with a 100-year time horizon (GWP100a), *marine eutrophication*, *terrestrial acidification*, and *water consumption* are reported for a functional unit of 1 kg of processed films or nanofiber mats.

2.8. Statistical analysis

The statistical analysis of the mechanical properties and size distribution was performed using a one-way analysis of variance (ANOVA) and a *t*-test with α 0.05. The statistical analysis of contact angle measurements (results of wettability) was performed using Two-way ANOVA with level of significance of 0.05.

3. Results and discussion

3.1. Processing and morphology of films and nanofibrous mats

Colloidal chitin nanofibrils were isolated from the white mushroom using a top-down approach that combines mild mechanical (home blender) and chemical treatments (aqueous 1 M NaOH). The isolated material was characterized physico-chemically and morphologically, as summarized in Fig. 2. As indicated by the attenuated total reflectance-Fourier transform infrared spectroscopy (ATR-FTIR) and X-ray diffraction (XRD), ChNFs present the characteristic features of α -chitin, with absorption bands at $3650\text{--}3200 \text{ cm}^{-1}$ ($-\text{OH}$ stretching), the amide I (1628 cm^{-1}), II (1556 cm^{-1}), and III (1315 cm^{-1}) bands that confirm the presence of chitin rather than chitosan, the CH_3 symmetrical deformation at 1378 cm^{-1} , and the C–O stretching at 1029 cm^{-1} [16,33]. The isolated material exhibits a semicrystalline character as confirmed by the two broad crystalline peaks centered at $2\theta = 9.2^\circ$ and 19.7° , together with a shoulder at $2\theta = 20.5$, corresponding to the (020), (110) and (120) planes of α -chitin, respectively. A crystallinity degree of $\sim 59\%$ is estimated according to the intensity of the (020) reflection [51]. In addition, the relatively low intensity of the amide bands in FTIR, together with a broad bump in XRD indicates the presence amorphous β -glucans in the material, estimated to be $\sim 56 \text{ wt}\%$ based on our previous analyses [51]. The presence of α -chitin and β -glucans is further confirmed by the ^{13}C NMR spectrum in Fig. 2c, with characteristic signals at 174 ppm for C=O (chitin), 23 ppm for CH_3 (chitin), no doublets for C4/C6 (indicating the occurrence of chitin rather than chitosan), and a smaller signal at 33 ppm from (1 \rightarrow 3)- β -D-glucans [52]. Additionally, an *N*-acetylation degree of 76 % is estimated according to the integral of methyl carbon (CH_3 signal at 22.8 ppm) normalized to the integrals of all the carbon groups in the D-glucopyranosyl ring (C1 to C6). Finally, the TEM image in Fig. 2d reveals a fibrillar structure of individual ChNFs, with lengths extending up to $1 \mu\text{m}$ and diameters above 20 nm. ChNF bundles could be also observed due to a strong hydrogen bonding upon sample preparation (drying of an aqueous dispersion drop onto a hydrophilic carbon grid). The length and diameter of individual ChNFs observed under TEM are above the values reported for α -chitin crystallites (2–5 nm and $\sim 300 \text{ nm}$, respectively), suggesting that ChNFs may be composed upon the assembly of more than the conventional 18–25 chitin molecular chains of single α -chitin crystallites together with glucans [16]. For comparison, acid hydrolysis of king crab endocuticles or lobster exoskeletons yields nanochitin with a diameter of 10–18 nm and a length of 300–500, while the acid hydrolysis of shrimp shells results in nanochitin with a diameter of 10–50 nm and a length of 50–300 nm [26]. Such dimensions are in general larger than the 9–17 nm width and 150–300 nm length observed for cellulose nanocrystals

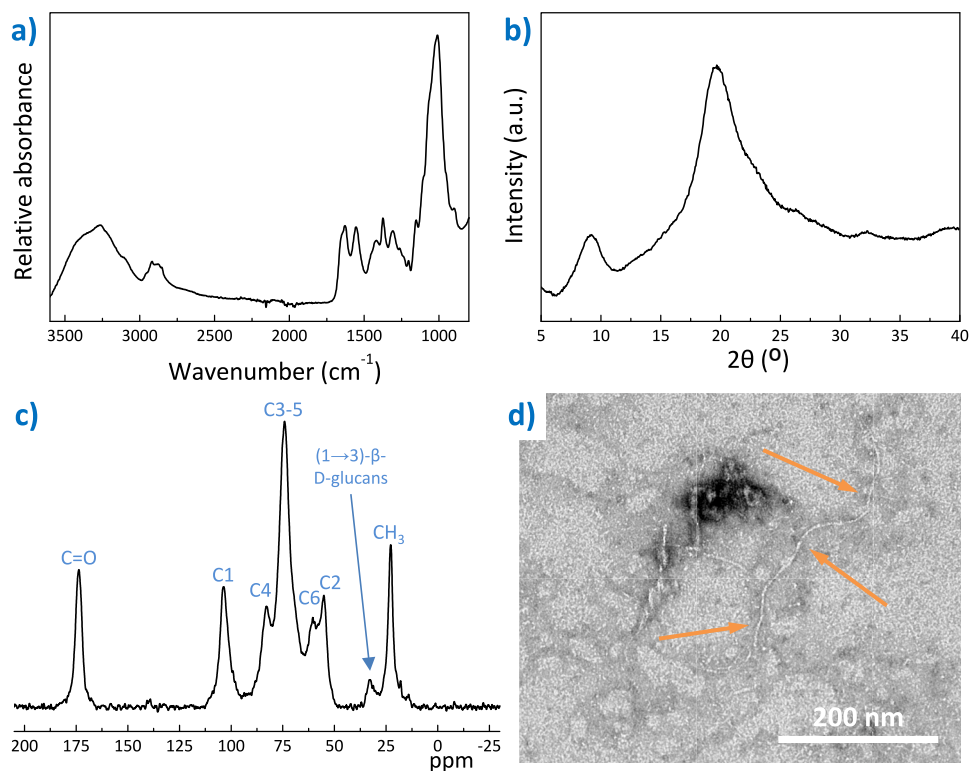


Fig. 2. Fungal ChNF characterization: (a) ATR-FTIR spectrum; (b) XRD pattern; (c) ^{13}C NMR spectrum and (d) transmission electron microscopy (TEM) image. An individual ChNF is highlighted by orange arrows.

isolated upon sulphuric acid hydrolysis of cellulose [53].

The materials were processed by SBS under the conditions outlined in Table 1 following our previously optimized process [38,46]. The specific processing parameters were considered based on the feasibility of carrying out the SBS process. This includes uninterrupted injection

and ejection of polymer solution through the nozzle, as well as ensuring there is no polymer accumulation at the tip of the needle that could cause blocking. Additionally, the overall stability of the solution blow spinning process was taken into account. To prepare the films, acetone and DMF were chosen due to their ability to obtain high outputs with

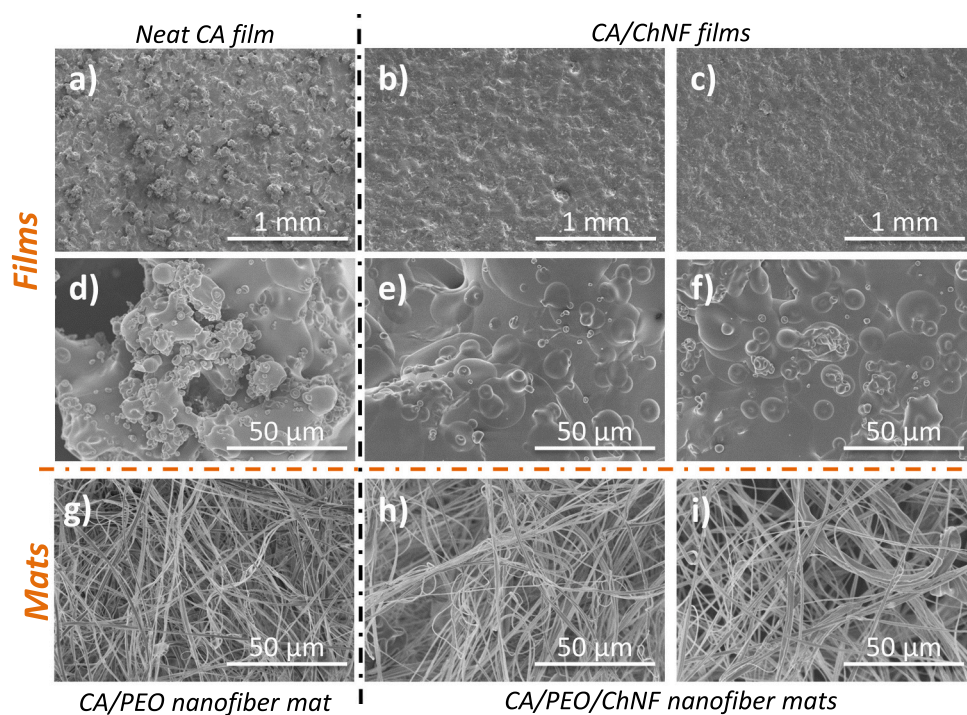


Fig. 3. Representative FE-SEM micrographs showing the surface morphology of: CA films (a, d); CA/ChNF films (b, e- 1.5 wt%; c, f- 2.5 wt% of ChNF); and CA/PEO nanofiber mats: (g) and CA/PEO/ChNF (h – 1 wt% and i- 2 wt% ChNF) nanofiber mats.

high injection rates [38]. Upon adding ChNFs to the CA solution, the injection rates and air pressure were reduced to maintain stability in the SBS process. We found that increasing the ChNF concentration above 2.5 wt% resulted in nozzle blocking. When processing the nanofibrous composite materials, similar but less pronounced effect occurred when 5 wt% of ChNFs was added to a polymer mixture of CA/PEO. Frequent nozzle blockages prevented the collection of a higher amount of material. Despite this, the collected sample was subjected to morphological, thermal and structural characterization. However, the maximum ChNF concentration to ensure completely stable and uninterrupted processing of the nanofibrous mat that can be collected in higher amounts is 2 wt%.

The morphology of the films and nanofibers mats was investigated using FE-SEM as presented in Fig. 3. While the CA-based films prepared by SBS resulted in macroscopically flat surfaces, the micrographs reveal distinctive surface features for neat CA and CA/ChNF films (Fig. 3a-f). At low magnifications, polymer beads that formed as a result of coalescence droplets during SBS can be observed. In contrast, the inclusion of ChNF seems to decrease the presence of those polymer beads, resulting in flatter and more uniform surfaces (larger portions of flat areas are seen at higher magnifications in Fig. 3e,f). This is supported by the surface roughness measurements presented in Fig. 4, where a significant decrease of arithmetic mean roughness parameter (R_a) is achieved upon ChNF addition. Specifically, the surface roughness on the top side, which is open to air during collecting in SBS, is reduced by 50 %. We propose that this reduction originates from the ChNFs acting as a binder to CA macromolecules and thereby improving film homogeneity. The presence of glucans that remain covalently attached to ChNF improves the cohesion and interfacial properties of the films [32]. On the other hand, the underside of the film shows a similar surface roughness for all the compositions, indicating that the polymer solution adopts the morphology of the collector during SBS process. Wettability measurements using water contact angle measurements showed that the inclusion of ChNF increases the wettability of the surfaces in close contact with the collector (bottom) as indicated by the reduction of the contact angle from 74° to $55\text{--}60^\circ$ (Fig. 4c). The wettability studies were only performed onto films because nanofibrous materials swell significantly

because of the presence of PEO component, which dissolves changing the final morphology of the material [46]. A two-way ANOVA analysis showed that both the side of the sample and concentration of added ChNF influence significantly the wettability of materials.

The morphology of nanofibers spun with and without ChNFs in Fig. 3 g-i do not show significant differences. All the samples present uniform and defect-free features. The size distributions in terms of nanofiber diameters for all the ChNF compositions are given in Fig. 5, with additional statistical data provided in Table S2. The addition of 1 wt% ChNF reduces the nanofiber diameter from 591 ± 251 nm (neat CA) to 532 ± 200 nm. Increasing the ChNF concentration to 2 wt% results in larger diameter values of 568 ± 266 nm. Although these differences fall within standard deviation values, further statistical analysis using ANOVA reveals statistically significant differences with values of $p < 0.05$ for all samples. The addition of 5 wt% ChNF leads to broadening of the distribution and an increase in the mean size to 676 ± 280 nm. To gain additional insights into the size distribution, we also considered the mode and median values (Table S2) [46]. The mode is consistent across all samples except for NF/ChNF 1, which also shows the lowest values for all distribution parameters. In contrast, the mean and median values are the highest for the NF/ChNF 3 sample. This suggests that adding ChNFs at low concentrations of 1 wt% reduces nanofiber diameters, while higher ChNF concentrations enlarge the diameter of the nanofibers. It is important to note the lower nanofiber diameters obtained in this study compared to the previous study [46], where a 12 % w/v CA solution was used for polymer mixture preparation, as opposed to the 10 % w/v CA used here. The maximum ChNF concentration to ensure uninterrupted processing of the nanofibrous mat was found to be 2 wt%.

3.2. Structural and conformational features

X-ray diffraction (XRD) can provide information on the semi-crystalline structure of polymeric films and nanofiber mats. This has direct implications in fields such as energy storage [54] and packaging [55]. The diffractograms in Fig. 6a for films are characterized by two main broad peaks centered at $2\theta = 10.1^\circ$ and 17.4° , while the nanofiber

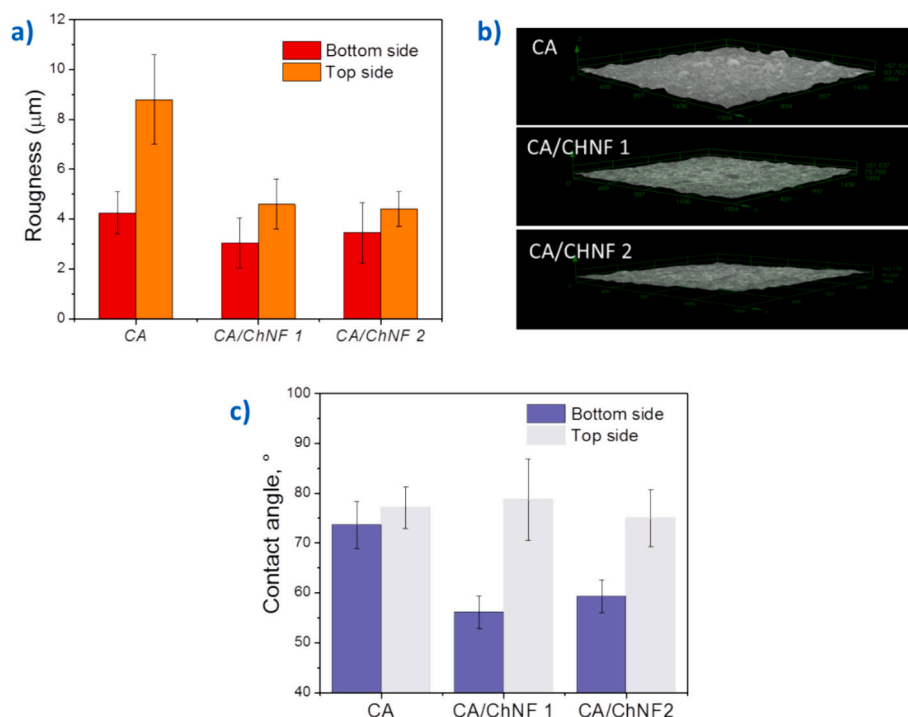


Fig. 4. (a) Arithmetic mean roughness (R_a) on both sides of neat CA and CA/ChNF composite films with (b) representative 3D images of the top surface of the films and (c) corresponding contact angles with water.

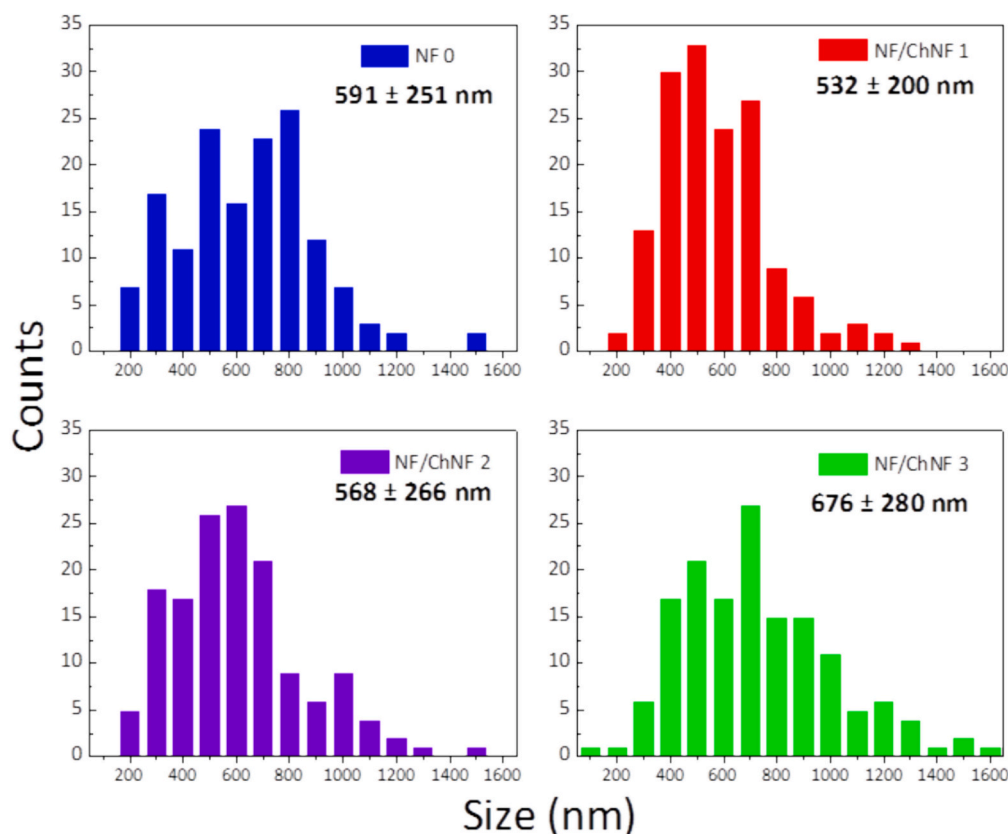


Fig. 5. Size distribution of (a) neat CA/PEO nanofibers, (b-d) composites CA/PEO/ChNF nanofibers with different concentration of ChNF filler.

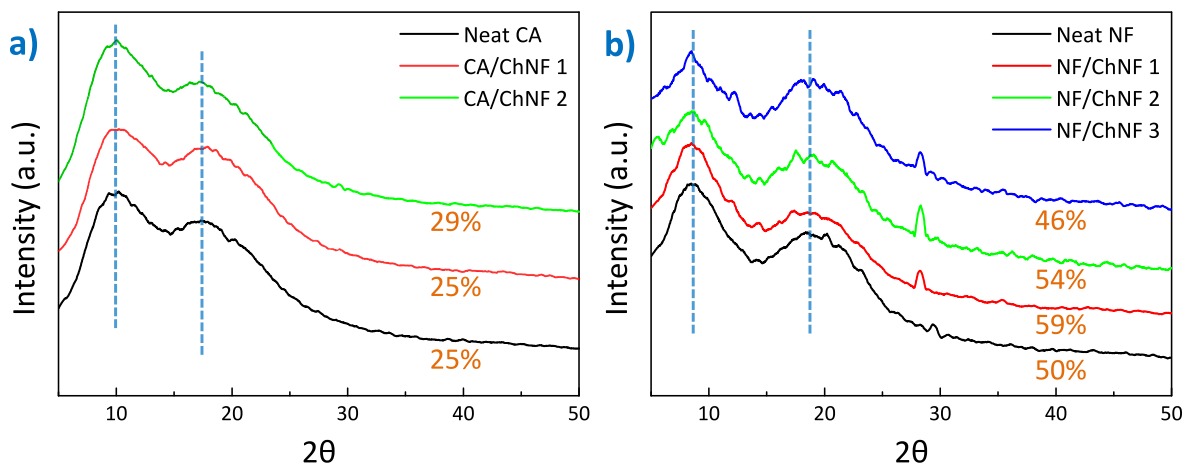


Fig. 6. XRD patterns of (a) CA/ChNF films and (b) CA/PEO/ChNF nanofiber mats. The position of the diffraction peaks is highlighted by a dotted blue line. Crystallinity degree values are shown in orange. (For interpretation of the references to colour in this figure legend, the reader is referred to the web version of this article.)

mats in Fig. 6b present the two broad peaks at $2\theta = 8.5^\circ$ and 18.7° . The diffraction peaks suggest the presence of cellulose triacetate moieties [56]. In contrast, four sharper diffraction peaks are observed at $2\theta = 14.9, 16.5, 22.7$ and 34.4° corresponding to the presence of the planes $(1\bar{1}\bar{1}0)$, (110) , (200) , and (004) for cellulose I β (Avicel) [57,58]. The diffractograms of the films and nanofiber mats correlate well with the results obtained for cellulose triacetate I and II structures [59]. Small differences may be explained by the different solvents used for processing and the fact that the acetate used in this work is not triacetate but one CA with a DS of 2.45. Besides, the larger intensity of the first diffraction peak over the second one indicates a high degree of

substitution with a large presence of acetyl groups [60]. There are no differences in peak position between the films and mats, indicating that the inter-atomic spacing (d -spacing, Bragg's law) is not modified by the presence of ChNFs [61]. No ChNF diffraction peaks at $2\theta = 9.2$ and 19.7° originating from the (020) and (110) of α -chitin is seen given the low concentration of these bio-colloids in the material [34].

Additionally, the two diffraction peaks are found superimposed over a broad amorphous halo, which indicates the coexistence of crystalline and amorphous regions within the samples. To quantify the degree of crystallinity, a peak deconvolution was used to separate the amorphous and crystalline contributions in the diffraction pattern. The

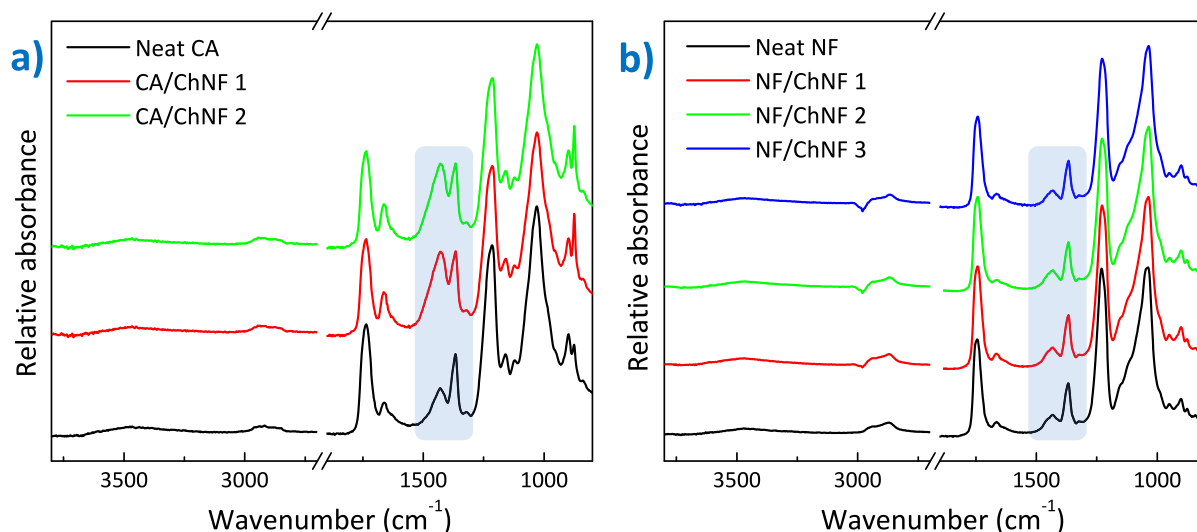


Fig. 7. ATR-FTIR spectra of (a) CA/ChNF films and (b) CA/PEO/ChNF nanofiber mats. Spectra are normalized to the peak with the highest intensity at 1035 cm^{-1} .

deconvoluted XRD patterns of ChNF-reinforced CA films and nanofiber mats are shown in Fig. S2. This approach was chosen due to its higher accuracy compared to other methods such as the Segal method, which solely considers the heights of the 002 peak and the minimum found between 002 and 101 peaks [62]. Crystallinity degrees (orange highlighted in Fig. 6) range from 25 to 59 % depending on the sample. The low crystallinities of the samples when compared to Avicel cellulose (which has crystallinity degrees of 57–92 %) [62], originate from the substitution of the cellulosic hydroxyl groups by acetyl groups, which have a greater volume and enlarge the interfibrillar distances and thus increase the disorder [63]. However, both the film and nanofiber mats show a slight increase in crystallinity when reinforced with ChNF at intermediate concentrations. This increase may be beneficial in achieving materials with greater stiffness.

Attenuated total reflectance-Fourier transform infrared (ATR-FTIR)

experiments were conducted to identify the occurrence of specific interactions between the CA matrix and ChNFs. The ATR-FTIR spectra in Fig. 7a and Fig. 7b show the characteristic absorption bands of cellulose acetate for all compositions, with the cellulose backbone identified at approximately 1035 cm^{-1} (symmetric C-O-C stretching). The intensity of the band at $3650\text{--}3200\text{ cm}^{-1}$ originating from the non-esterified -OH groups, notably decreases when compared to native cellulose. This indicates a disruption of hydrogen bonding in the material. The chemical conversion to an ester is confirmed by the appearance of the band at 1735 cm^{-1} , which corresponds to the C=O stretching of the acetyl group. Additionally, the bands corresponding to C-H bending and C-O stretching vibrations of acetyl groups are seen at 1370 cm^{-1} and 1220 cm^{-1} , respectively [56]. The bands at 2920 cm^{-1} (ν_{CH}) and 904 cm^{-1} (acetate methyl groups) are also characteristic of cellulose triacetate. The differences between films and nanofiber mats are mainly observed

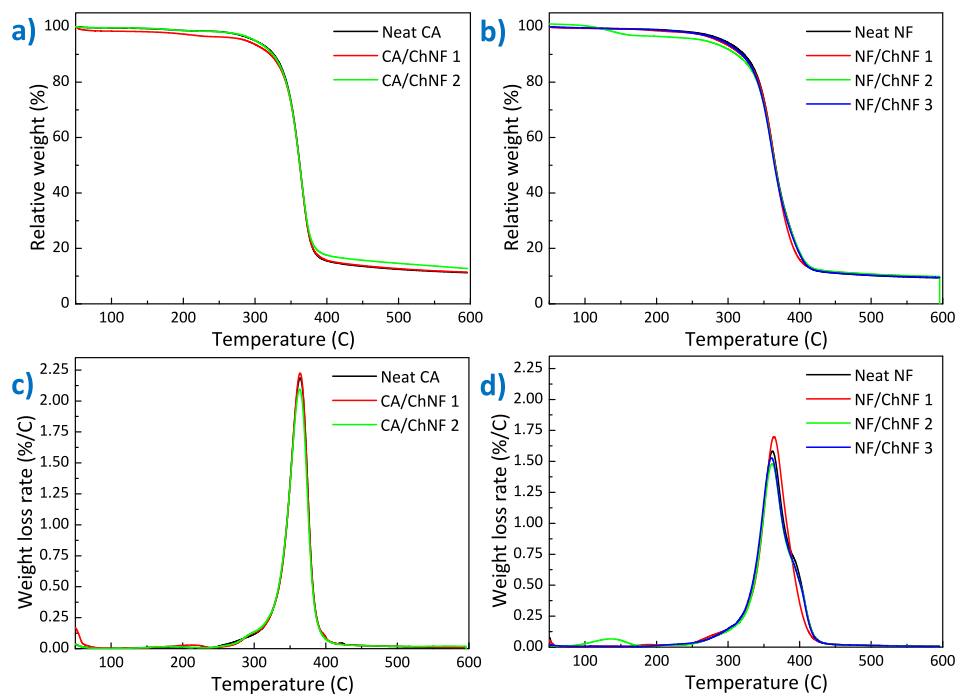


Fig. 8. Thermogravimetric traces of (a) CA/ChNF films and (b) CA/PEO/ChNF nanofiber mats at a heating rate of $10\text{ }^{\circ}\text{C}\cdot\text{min}^{-1}$ under N_2 atmosphere and their corresponding weight lost rates in (c) and (d), respectively.

Table 2Characteristic thermodegradation temperatures ($T_{5\%}$ and T_{peak}) and maximum degradation rates (α_{max}) of CA/ChNF films and CA/PEO/ChNF nanofiber mats.

Sample	$T_{5\%}$ (°C)	T_{peak} (°C)	α_{max} (%/°C)
CA-F	299.8	364.1	2.18
CA-F-ChNF 1	287.4	364.1	2.23
CA-F-ChNF 2	299.9	363.7	2.10
NF 0	294.2	362.0	1.58
NF-ChNF 1	286.4	364.2	1.70
NF-ChNF 2	288.2	361.3	1.42
NF-ChNF 3	290.4	360.8	1.53

in the bands that correlate with the crystallinity of the cellulose acetate. As highlighted in blue in Fig. 7a and Fig. 7b, an increased intensity is observed for the band located at 1428 cm^{-1} with the increase of ChNF concentration. This band originates from the symmetric δ_{CH_2} at C-6 in the crystalline phase. Likewise, the intensity of the band at 897 cm^{-1} decreases its intensity (δ_{CH_2} , amorphous region). In contrast, the bands remain unchanged in the nanofiber mat. These results suggest that the presence of ChNFs induces an increase in crystallinity for the films, while no changes in crystallinity are observed for the nanofiber mats.

3.3. Thermal stability of composite films and nanofibrous mats

The thermal stability of polymers is a key property to consider for their practical implementation. A poor thermal stability can yield to a loss in the material thermo-mechanical properties, limiting its use in load-bearing or packaging applications. This is particularly true for polysaccharides, which show higher sensitivity to temperature in comparison with their petro-based counterparts. The thermodegradation of CA/ChNF films and CA/PEO/ChNF nanofiber mats was studied by thermogravimetric analysis (TGA) under a N_2 atmosphere. The TGA curves and weight loss rates are shown in Fig. 8, while Table 2

summarizes the characteristic thermodegradation temperatures and maximum degradation rates for all the materials. No signs of DMF or Ac evaporation were observed at temperatures up to $200\text{ }^\circ\text{C}$, indicating that the developed materials are free of occluded solvent. All materials exhibit high thermal stability due to the presence of acetyl groups. Specifically, a single thermodegradation process occurs centered at approximately $365\text{ }^\circ\text{C}$, resulting in an 85 wt% loss. This process is caused by the breakdown of glycosidic bonds in the cellulose backbone, dehydration and depolymerization, and subsequent loss of acetate groups [64,65]. At temperatures above $400\text{ }^\circ\text{C}$, a smoother degradation process occurs, transforming the remaining cellulosic material into carbon residues [66]. Finally, a char equivalent of approximately 11 wt% at $600\text{ }^\circ\text{C}$ is achieved. This char equivalent increases by nearly 2 wt% in the presence of ChNFs, indicating the degradation and subsequent carbonization of 2-amino-2-deoxy-D-glucopyranose units (for chitin) and the glucans [34,67].

The onset of thermal degradation of CA film, determined as the temperature at which the first 5 % weight loss occurs, is lowered by $12\text{ }^\circ\text{C}$ upon 1 wt% ChNF addition. Similarly, the thermodegradation of nanofiber mats initiates at lower temperatures in the presence of ChNFs. These observations suggest an accelerated thermodegradation at early

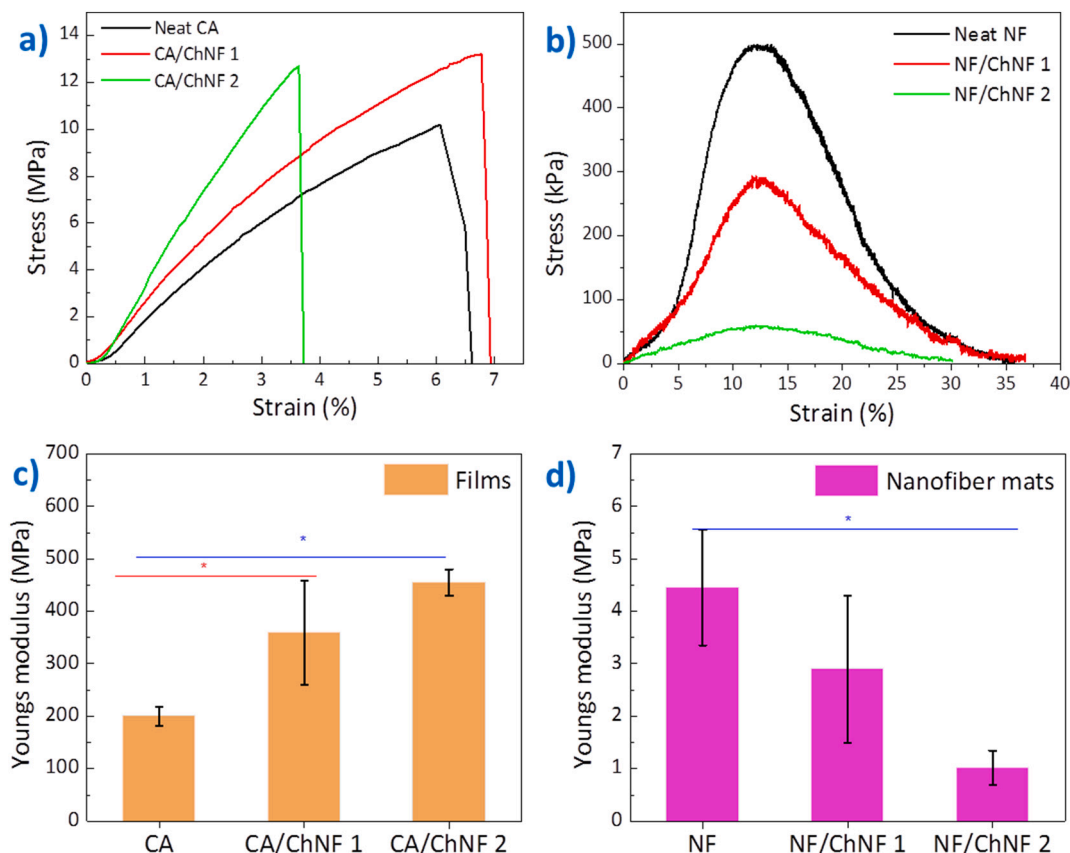


Fig. 9. Representative stress-strain curves of films (a) and nanofibers (b) and their Young's modulus (c and d), respectively.

stages of degradation due to the lower thermal stability of ChNFs over CA. Nevertheless, the peak degradation temperature remains approximately at 363 °C for all compositions studied with slight variations in weight loss rates, indicating that the overall thermal stability of neat CA is minimally affected by ChNF incorporation. This finding has relevant implications, particularly when considering the results observed for other bio-colloids such as CNCs. In these cases, the surface sulfate half-ester groups catalyze thermodegradation events of the polymeric matrix, reducing the overall thermal stability of the composite materials [68,69].

3.4. Mechanical properties of composite films and nanofibrous mats

The mechanical response of materials is of special interest for the application of films and fibers, as it determines their area of application. Nanofillers are often added to polymers to reinforce the matrix and improve the material's stability over time. Therefore, the mechanical properties of the materials were analyzed by uniaxial tensile testing. Fig. 9a and Fig. 9b show the representative stress–strain curves for films and nanofiber mats, respectively, while Fig. 9c and Fig. 9d summarize the average and standard deviation of the Young's modulus. The films exhibit a brittle behavior, with a failure characterized by a sharp drop in strength and elongation at break values below 10 %. On the contrary, nanofiber mats exhibit a behavior that could be considered ductile, as their elongation at break values are above 30 %. However, there is no clear evidence of plastic deformation of the materials. Instead, the observed failure is characterized by a smooth drop of mechanical strength. The curves in Fig. 9b do not show the typical catastrophic failure of polymeric materials, but rather a slow decrease in tensile strength, as if gradual failure is occurring.

Table S3 presents the ultimate tensile strength (maximum stress at break), the strain at break, and Young's modulus for films and nanofibrous composites with ChNF concentrations up to 2.5 wt% and 2 wt%, respectively. The films have higher ultimate tensile strength values in the range of MPa, while nanofiber mats have breaking strength in the kPa range. The Young's modulus of films is affected by the addition of both concentrations of ChNF while in the case of nanofibers, statistically significant difference exists between sample without ChNF and with 2 wt% ChNF. The obtained values for nanofiber mats are comparable to

those reported in the literature for electrospun CA nanofibrous mats [11,13]. It is noteworthy that the addition of ChNF to both films and nanofiber mats had opposite effects on the resulting maximum stress at break and Young's modulus. In fact, ChNF incorporation to CA films increases the stiffness of the material. With the addition of 1.5 wt% ChNFs, the tensile strength and Young's modulus increase by 84 % and 80 %, respectively. Importantly, the ductility of the material is improved as reflected by the increase on the strain at break from 5.4 ± 2.3 % to 7.8 ± 3.0 %. However, further incorporation of ChNFs appears to have a detrimental effect. The reduction in ultimate tensile strength is due to the increased presence of ChNF, which can create weak spots in the nanocomposite structure. This can eventually lead to a reduced breaking strength and early failure compared to the CA/ChNF1 sample [70]. The increase in CA films strength upon the addition of ChNF can be attributed to the increased matrix crystallinity, as determined by ATR-FTIR and XRD. In contrast, nanofiber mats exhibit an opposing behavior, whereby even low ChNF concentrations significantly decrease the tensile strength and Young's modulus. This reduction in tensile strength may be due to the addition of ChNF disrupting the entanglement of CA/PEO nanofibers. However, the elasticity is maintained as evidenced by the slight decrease in strain at break and the ability of the material to withstand stretching. Although the nanofibrous mat with 5 wt% ChNF was produced using DBD, the small amount of material collected made it unfeasible to assess its mechanical properties.

A graphical representation of plausible mechanism that lies behind the observed ductility of CA/PEO/ChNF composite nanofibers, is given in Fig. 10 and consists of three stages. In the first stage of tensile testing (*stage I*), the nanofibers remain randomly oriented. Upon external stress application (*stage II*), a necking effect occurs, and the majority of the CA/PEO nanofibers align along the direction of the applied stress due to external mechanical forces. Finally (*stage III*), the materials undergo progressive fracture events associated with the fibers as individual entities. The stress-strain curves show a stress approaching zero kPa. However, new connections and bridging sites at the fractured regions may be present due to interfacial interactions between the matrix and the ChNFs, presenting a small resistance to the applied stress and preventing the sudden failure of the material.

Similar results in terms of maximum strength and gradual strength decrease after fracture have been reported [11,71]. This characteristic

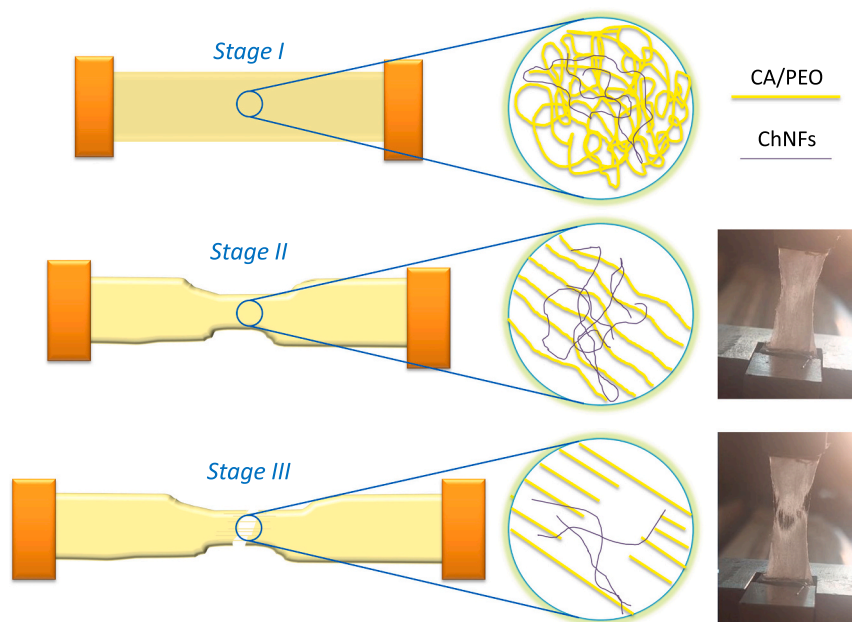


Fig. 10. Graphical representation of the proposed tensile testing behavior of nanofibrous composites.

may be important for materials that require ductility, or at least avoiding the catastrophic failure to allow for decisions to be made before fatal consequences occur. This is particularly relevant for biomedical scaffolds and other biomedical applications (wound dressing, tissue engineering), where polysaccharide-based materials hold a bright future [8,11,72].

3.5. Environmental impacts according to life cycle assessment

Life cycle assessment (LCA) methodology has been applied to quantify, for the first time, the environmental impacts of SBS processing. Details on the modeled inventory are given in Tables S1 and S4, while the resulting *cradle-to-gate* environmental impacts per 1 kg of processed material are summarized in Fig. 11. Results include the impact categories of global warming potential with over 100-year time horizon, marine eutrophication, terrestrial acidification and water consumption. Overall, the films show reduced environmental impacts compared to the nanofiber mats, with GWP values of 69.7–173.4 kg-CO₂-equiv. and 152.1–347.4 kg-CO₂-equiv. per kilo of fabricated material, respectively. Although these values remain well above the carbon footprint shown by commercial petroleum-based polymers (2.0 to 16.6 kg-CO₂-equiv.·kg⁻¹ for polypropylene, polyethylene, polystyrene, polycarbonate, or polyvinylfluoride), the obtained CO₂ footprint remains below the majority of polymer nanocomposites based on carbon nanofibers, Ag nanoparticles, TiO₂ nanoparticles, and even nanocelluloses [73]. Moreover, these results also prove the potential of SBS to obtain nanofibers, which could later be used as reinforcing agents in polymer matrices, at relatively low environmental cost compared to processes involving homogenization of cellulose fibers to obtain nanofibrillated cellulose (770–814 kg-CO₂-equiv.·kg⁻¹) [74].

In any case, the relatively high GWP results indicate the need for further process optimization in the near future. In this sense, the results can be explained by the increased energy demand for the processing of nanofiber mats, which requires on average 1.56 kWh·g⁻¹ compared to 0.84 kWh·g⁻¹ for film formation. Despite the relatively low impact of fungal nanochitin, significantly higher impacts are also observed for nanocomposites with increased concentration of ChNFs. However, this increase is due to a decrease in yield resulting from higher viscosities, which make processing more difficult, both for films and nanofiber mats (see Table S1 for the material and energy inventories). As a result, the overall resource efficiency of the process is lowered, increasing the impacts per amount of resulting material [75]. A similar trend is observed in the *terrestrial acidification* and *water consumption* categories, suggesting that the overall sustainability of the materials is determined by the fabrication process to reach specific material morphology (film vs. nanofiber mat), and ChNF concentration. However, it should be noted that the *marine eutrophication* is larger on the case of film processing. This result originates from the use of DMF during film processing, a solvent known to increase nitrogen levels in water bodies [76]. Altogether, these environmental results point towards future optimization, emphasizing the necessity of achieving a proper balance between solvent selecting, energy consumption, and material yield.

4. Conclusions

This study develops composite films and nanofiber mats containing renewable carbon. Specifically, cellulosic-matrices reinforced with chitin nanofibrils derived from fungi are developed, seeding new information to the growing field of fungal-derived materials. ChNFs are isolated from *Agaricus bisporus*, the common white mushroom by a top-

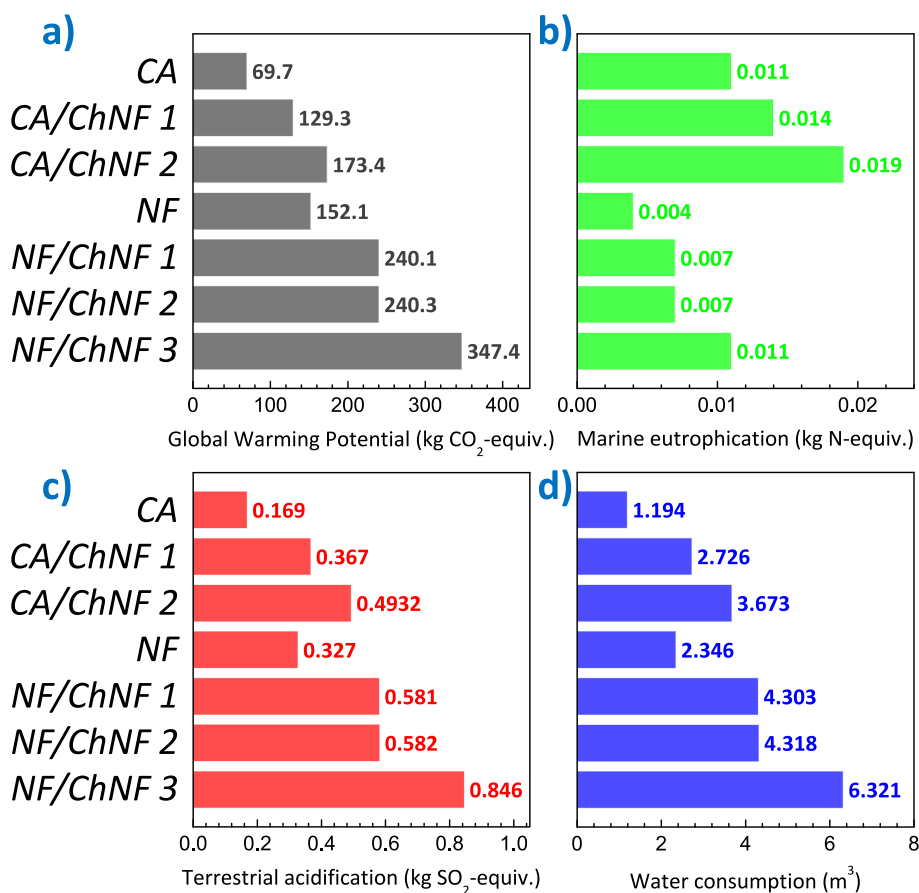


Fig. 11. Environmental impacts of fabricated CA/ChNF films and nanofiber mats per kilo of material in the categories of: (a) global warming potential; (b) marine eutrophication; (c) terrestrial acidification and (d) water consumption.

down approach. Unlike chitin sources from crustaceans, the process adopted involved a mild alkaline treatment to remove proteins and was assisted by a kitchen blender for fibrillation. Cellulose acetate is selected as a model renewable and biodegradable polymer with a widespread industrial application. Using solution blow spinning, a high-processing rate emerging technology, cellulose acetate/chitin nanofibrils free-standing films, and cellulose acetate/poly(ethylene oxide)/chitin nanofibrils nanofiber mats were obtained. ChNF incorporation can increase the crystallinity degree of composite films. The surface roughness of neat CA films is reduced from 8.8 μm to 4.4 μm when processed into CA/ChNF 2.5 wt% nanocomposite. This influenced the increased wettability of films, reflected in a decrease of contact angle with deionized water. Furthermore, thanks to the covalently linked β -D-glucans, ChNFs exhibit a significant mechanical reinforcing effect in CA films. The ultimate tensile strength increases from 8.2 ± 3.9 MPa for neat CA to 15.1 ± 4.10 MPa after the incorporation of 1.5 wt% ChNF. Conversely, in nanofibrous mats, the incorporation of ChNF into CA/PEO composite increases the ductility of material and prevents sudden failure upon applied mechanical stress. This increased ductility of nanofiber mats may be advantageous for biomedical applications. The proposed mechanism for explaining stress-strain curves in nanofibrous composites relies on increased interfacial interactions. These interactions originate from two factors: PEO envelopes CA nanofibers during production, while the presence of β -D-glucans in ChNFs acts as a binder. The materials produced in this work remain thermally stable up to 285 °C.

With global warming potential values from 69.7 to 347.4 kg-CO₂-equiv. $\cdot\text{kg}^{-1}$, life cycle assessment results point potential environmental benefits of solution blown cellulose acetate/chitin nanofibril materials when compared with analogous fibrillar-like materials. Altogether, these results demonstrate the potential of chitin nanofibrils derived from fungi to serve as reinforcing fillers in bio-based polymeric films, such as cellulose acetate using the solution blow spinning technique. This approach offers not only new possibilities for sustainable material development beyond nanocelluloses, but also provides a solution to use the same process to obtain versatile morphologies (continuous films and nanofibers) by changing the polymer mixtures. Further optimization of the SBS process should be done to additionally decrease the environmental impact, especially in terms of electricity consumption and increasing the process output.

CRediT authorship contribution statement

Ana Kramar: Writing – review & editing, Writing – original draft, Visualization, Project administration, Investigation, Funding acquisition, Formal analysis, Data curation, Conceptualization. **Javier González-Benito:** Writing – review & editing, Investigation, Funding acquisition, Formal analysis. **Nataša Nikolić:** Visualization, Investigation, Formal analysis, Data curation. **Aitor Larrañaga:** Investigation, Formal analysis, Data curation. **Erlantz Lizundia:** Writing – review & editing, Writing – original draft, Visualization, Supervision, Resources, Project administration, Investigation, Funding acquisition, Formal analysis, Data curation, Conceptualization.

Declaration of competing interest

The authors declare that they have no known competing financial interests or personal relationships that could have appeared to influence the work reported in this paper.

Data availability

The data supporting this work is shown in the Manuscript and the Supplementary material.

Acknowledgements

EL acknowledges the funds from the University of the Basque Country (Convocatoria de ayudas a grupos de investigación GIU21/010). The authors also acknowledge the Open Access funding provided by the University of Basque Country (UPV/EHU). Technical and human support provided by SGiker (UPV/EHU, MICINN, GV/EJ, EGEF, and ESF) is gratefully acknowledged. AK and JGB appreciate financial support by CONEX-Plus program of Universidad Carlos III de Madrid (UC3M) and the European Commission through the Marie-Sklodowska Curie COFUND Action (Grant Agreement No 801538). JGB and NN also appreciate the financial support received from AEI (Ministerio de Ciencia e Innovación of Spain, PID2020-112713RB-C22 and –C21); the Universidad Carlos III de Madrid, Fondos de Investigación de Fco. Javier González Benito [2012/00130/004] and the strategic Action in Multifunctional Nanocomposite Materials [Code: 2011/00287/003]. AL is thankful for funds from the Basque Government, Department of Education (IT-1766-22).

Appendix A. Supplementary data

Supplementary data to this article can be found online at <https://doi.org/10.1016/j.ijbiomac.2024.132046>.

References

- [1] J. Rockström, J. Gupta, D. Qin, S.J. Lade, J.F. Abrams, L.S. Andersen, D. I. Armstrong McKay, X. Bai, G. Bala, S.E. Bunn, D. Ciobanu, F. DeClerck, K. Ebi, L. Gifford, C. Gordon, S. Hasan, N. Kanie, T.M. Lenton, S. Loriani, D.M. Liverman, A. Mohamed, N. Nakicenovic, D. Obura, D. Ospina, K. Prodan, C. Rammelt, B. Sakschewski, J. Scholtens, B. Stewart-Koster, T. Tharammal, D. van Vuuren, P. H. Verburg, R. Winkelmann, C. Zimm, E.M. Bennett, S. Bringezu, W. Broadgate, P. A. Green, L. Huang, L. Jacobson, C. Ndehedehe, S. Pedde, J. Rocha, M. Scheffer, L. Schulte-Uebbing, W. de Vries, C. Xiao, C. Xu, X. Xu, N. Zafra-Calvo, X. Zhang, Safe and just earth system boundaries, *Nature* 619 (2023) 102–111, <https://doi.org/10.1038/s41586-023-06083-8>.
- [2] N. Seddon, A. Chausson, P. Berry, C.A.J. Girardin, A. Smith, B. Turner, Understanding the value and limits of nature-based solutions to climate change and other global challenges, *Philos. Trans. R. Soc. B Biol. Sci.* 375 (2020) 20190120, <https://doi.org/10.1098/rstb.2019.0120>.
- [3] T.D. Moshood, G. Nawansir, F. Mahmud, F. Mohamad, M.H. Ahmad, A. AbdulGhani, Sustainability of biodegradable plastics: new problem or solution to solve the global plastic pollution? *Curr. Res. Green Sustain. Chem.* 5 (2022) 100273 <https://doi.org/10.1016/j.crgsc.2022.100273>.
- [4] S. Gopi, A. Pius, R. Kargl, K.S. Kleinschek, S. Thomas, Fabrication of cellulose acetate/chitosan blend films as efficient adsorbent for anionic water pollutants, *Polym. Bull.* 76 (2019) 1557–1571, <https://doi.org/10.1007/s00289-018-2467-y>.
- [5] K. Harini, M. Sukumar, Development of cellulose-based migratory and nonmigratory active packaging films, *Carbohydr. Polym.* 204 (2019) 202–213, <https://doi.org/10.1016/j.carbpol.2018.10.018>.
- [6] H. Zhou, S. Zhou, X. Ji, Y. Zhao, Y. Lv, Y. Cheng, Y. Tao, J. Lu, J. Du, H. Wang, High-performance cellulose acetate-based gas barrier films via tailoring reduced graphene oxide nanosheets, *Int. J. Biol. Macromol.* 209 (2022) 1450–1456, <https://doi.org/10.1016/j.ijbiomac.2022.04.115>.
- [7] R. Konwarh, N. Karak, M. Misra, Electrospun cellulose acetate nanofibers: the present status and gamut of biotechnological applications, *Biotechnol. Adv.* 31 (2013) 421–437, <https://doi.org/10.1016/j.biotechadv.2013.01.002>.
- [8] Y.H. Song, E. Ji, K. Il Joo, J.H. Seo, Development of mechanically reinforced bioadhesive electrospun nanofibers using cellulose acetate–Levan complexes, *Cellulose* 30 (2023) 1685–1696, <https://doi.org/10.1007/s10570-022-04971-2>.
- [9] G. El-Barbary, M.K. Ahmed, M.M. El-Desoky, A.M. Al-Enizi, A.A. Allothman, A. M. Alotaibi, A. Nafady, Cellulose acetate nanofibers embedded with Ag nanoparticles/CdSe/graphene oxide composite for degradation of methylene blue, *Synth. Met.* 278 (2021) 116824, <https://doi.org/10.1016/j.synthmet.2021.116824>.
- [10] G. Kumar, F.G. Khan, M.I. Abro, U. Aftab, A.W. Jatoti, Development of cellulose acetate/CuO/AgNP nanofibers based effective antimicrobial wound dressing, *Compos. Commun.* 39 (2023) 101550, <https://doi.org/10.1016/j.coco.2023.101550>.
- [11] A.A. Challa, N. Saha, P.K. Szewczyk, J.E. Karbowniczek, U. Stachewicz, F. A. Ngwabebhoh, P. Saha, Graphene oxide produced from spent coffee grounds in electrospun cellulose acetate scaffolds for tissue engineering applications, *Mater. Today Commun.* 35 (2023) 105974, <https://doi.org/10.1016/j.mtcomm.2023.105974>.
- [12] C. Wang, Y. Zhan, Y. Wu, X. Shi, Y. Du, Y. Luo, H. Deng, TiO₂/rectorite-trapped cellulose composite nanofibrous mats for multiple heavy metal adsorption, *Int. J. Biol. Macromol.* 183 (2021) 245–253, <https://doi.org/10.1016/j.ijbiomac.2021.04.085>.

- [13] E. Esmaeili, T. Eslami-Arshaghi, S. Hosseinzadeh, E. Elahirad, Z. Jamalpoor, S. Hatamie, M. Soleimani, The biomedical potential of cellulose acetate/polyurethane nanofibrous mats containing reduced graphene oxide/silver nanocomposites and curcumin: antimicrobial performance and cutaneous wound healing, *Int. J. Biol. Macromol.* 152 (2020) 418–427, <https://doi.org/10.1016/j.ijbiomac.2020.02.295>.
- [14] A.A. Aly, M.K. Ahmed, Nanofibers of cellulose acetate containing ZnO nanoparticles/graphene oxide for wound healing applications, *Int. J. Pharm.* 598 (2021) 120325, <https://doi.org/10.1016/j.ijpharm.2021.120325>.
- [15] K.H. Jang, Y.O. Kang, T.S. Lee, W.H. Park, Photocatalytic activities of cellulose-based nanofibers with different silver phases: silver ions and nanoparticles, *Carbohydr. Polym.* 102 (2014) 956–961, <https://doi.org/10.1016/j.carbpol.2013.10.036>.
- [16] L. Bai, L. Liu, M. Esquivel, B.L. Tardy, S. Huan, X. Niu, S. Liu, G. Yang, Y. Fan, O. J. Rojas, Nanochitin: chemistry, structure, assembly, and applications, *Chem. Rev.* 122 (2022) 11604–11674, <https://doi.org/10.1021/acs.chemrev.2c00125>.
- [17] T. Li, C. Chen, A.H. Brozyna, J.Y. Zhu, L. Xu, C. Driemeier, J. Dai, O.J. Rojas, A. Isogai, L. Wågberg, L. Hu, Developing fibrillated cellulose as a sustainable technological material, *Nature* 590 (2021) 47–56, <https://doi.org/10.1038/s41586-020-03167-7>.
- [18] F. Huang, X. Wu, Y. Yu, Y. Lu, Q. Chen, Acylation of cellulose nanocrystals with acids/trifluoroacetic anhydride and properties of films from esters of CNCs, *Carbohydr. Polym.* 155 (2017) 525–534, <https://doi.org/10.1016/j.carbpol.2016.09.010>.
- [19] S. Raghunath, M. Hoque, E.J. Foster, On the roles of cellulose nanocrystals in fiber cement: implications for rheology, hydration kinetics, and mechanical properties, *ACS Sustain. Chem. Eng.* (2023), <https://doi.org/10.1021/acssuschemeng.3c01392>.
- [20] A.B. Perumal, R.B. Nambiar, J.A. Moses, C. Anandharamakrishnan, Nanocellulose: recent trends and applications in the food industry, *Food Hydrocoll.* 127 (2022) 107484, <https://doi.org/10.1016/j.foodhyd.2022.107484>.
- [21] S. Sultan, G. Siqueira, T. Zimmermann, A.P. Mathew, 3D printing of nano-cellulosic biomaterials for medical applications, *Curr. Opin. Biomed. Eng.* 2 (2017) 29–34, <https://doi.org/10.1016/j.cobme.2017.06.002>.
- [22] N. Mittal, A. Ojanguren, N. Cavaşin, E. Lizundia, M. Niederberger, Transient rechargeable battery with a high lithium transport number cellulosic separator, *Adv. Funct. Mater.* 31 (2021) 2101827, <https://doi.org/10.1002/adfm.202101827>.
- [23] S. Liu, S.A. Qamar, M. Qamar, K. Basharat, M. Bilal, Engineered nanocellulose-based hydrogels for smart drug delivery applications, *Int. J. Biol. Macromol.* 181 (2021) 275–290, <https://doi.org/10.1016/j.ijbiomac.2021.03.147>.
- [24] E.J. Foster, R.J. Moon, U.P. Agarwal, M.J. Bortner, J. Bras, S. Camarero-Espinosa, K.J. Chan, M.J.D. Clift, E.D. Cranston, S.J. Eichhorn, D.M. Fox, W.Y. Hamad, L. Heux, B. Jean, M. Korey, W. Nieh, K.J. Ong, M.S. Reid, S. Renneker, R. Roberts, J.A. Shatkin, J. Simonsen, K. Stinson-Bagby, N. Wanasekara, J. Youngblood, Current characterization methods for cellulose nanomaterials, *Chem. Soc. Rev.* 47 (2018) 2609–2679, <https://doi.org/10.1039/C6CS00895J>.
- [25] P. Phanthong, P. Reubroycharoen, X. Hao, G. Xu, A. Abudula, G. Guan, Nanocellulose: extraction and application, *Carbon Resour. Convers.* 1 (2018) 32–43, <https://doi.org/10.1016/j.crcon.2018.05.004>.
- [26] E. Lizundia, T.-D. Nguyen, R.J. Winnick, M.J. MacLachlan, Biomimetic photonic materials derived from chitin and chitosan, *J. Mater. Chem. C* 9 (2021), <https://doi.org/10.1039/d0tc05381c>.
- [27] A. Narkevicius, L.M. Steiner, R.M. Parker, Y. Ogawa, B. Frka-Petesic, S. Vignolini, Controlling the self-assembly behavior of aqueous chitin nanocrystal suspensions, *Biomacromolecules* 20 (2019) 2830–2838, <https://doi.org/10.1021/acs.biomac.9b00589>.
- [28] Q. Jiang, Y. Ni, Q. Zhang, J. Gao, Z. Wang, H. Yin, Y. Jing, J. Wang, Sustainable nitrogen self-doped carbon nanofibers from biomass chitin as anodes for high-performance lithium-ion batteries, *Energy Fuel* 36 (2022) 4026–4033, <https://doi.org/10.1021/acs.energyfuels.2c00157>.
- [29] C.C. Satam, C.W. Irvin, A.W. Lang, J.C.R. Jallorina, M.L. Shofner, J.R. Reynolds, J. C. Meredith, Spray-coated multilayer cellulose nanocrystal–chitin nanofiber films for barrier applications, *ACS Sustain. Chem. Eng.* 6 (2018) 10637–10644, <https://doi.org/10.1021/acssuschemeng.8b01536>.
- [30] M.D. Lenardon, C.A. Munro, N.A.R. Gow, Chitin synthesis and fungal pathogenesis, *Curr. Opin. Microbiol.* 13 (2010) 416–423, <https://doi.org/10.1016/j.mib.2010.05.002>.
- [31] M. Berroci, C. Vallejo, E. Lizundia, Environmental impact assessment of chitin nanofibril and nanocrystal isolation from fungi, shrimp shells and crab shells, *ACS Sustain. Chem. Eng.* 10 (2022) 14280–14293, <https://doi.org/10.1021/acssuschemeng.2c04417>.
- [32] W.M.F.W. Nawawi, K.-Y. Lee, E. Kontturi, R.J. Murphy, A. Bismarck, Chitin nanopaper from mushroom extract: natural composite of nanofibers and glucan from a single biobased source, *ACS Sustain. Chem. Eng.* 7 (2019) 6492–6496, <https://doi.org/10.1021/acssuschemeng.9b00721>.
- [33] N. Yousefi, M. Jones, A. Bismarck, A. Mautner, Fungal chitin-glucan nanopapers with heavy metal adsorption properties for ultrafiltration of organic solvents and water, *Carbohydr. Polym.* 253 (2021) 117273, <https://doi.org/10.1016/j.carbpol.2020.117273>.
- [34] D. Ruiz, V.F. Michel, M. Niederberger, E. Lizundia, Chitin nanofibrils from fungi for hierarchical gel polymer electrolytes enabling transient zinc ion batteries with stable Zn electrodeposition, *Small* 19 (2023) 2303394, <https://doi.org/10.1002/smll.202303394>.
- [35] E. Lizundia, C.M. Costa, R. Alves, S. Lanceros-Méndez, Cellulose and its derivatives for lithium ion battery separators: a review on the processing methods and properties, *Carbohydr. Polym. Technol. Appl.* 1 (2020) 100001, <https://doi.org/10.1016/j.carpta.2020.100001>.
- [36] M.M. Castillo-Ortega, D. Hernández-Martínez, I. Santos-Sauceda, D.F. Plascencia-Martínez, J. Alvarado-Ibarra, J.L. Cabellos-Quiroz, Y.I. Cornejo-Ramírez, Electrospun cellulose acetate membranes coated with polypyrrole and their potential application in the recovery of metals, *ACS Omega* 7 (2022) 31059–31068, <https://doi.org/10.1021/acso.2c03129>.
- [37] H. Samadian, S. Zamiri, A. Ehterami, S. Farzambar, A. Vaez, H. Khastar, M. Alam, A. Ai, H. Derakhshankhah, Z. Allahyari, A. Goodarzi, M. Salehi, Electrospun cellulose acetate/gelatin nanofibrous wound dressing containing berberine for diabetic foot ulcer healing: in vitro and in vivo studies, *Sci. Rep.* 10 (2020) 8312, <https://doi.org/10.1038/s41598-020-65268-7>.
- [38] A. Kramar, J. González-Benito, Preparation of cellulose acetate film with dual hydrophobic-hydrophilic properties using solution blow spinning, *Mater. Des.* 227 (2023) 111788, <https://doi.org/10.1016/j.matdes.2023.111788>.
- [39] J.L. Daristotle, A.M. Behrens, A.D. Sandler, P. Kofinas, A review of the fundamental principles and applications of solution blow spinning, *ACS Appl. Mater. Interfaces* 8 (2016) 34951–34963, <https://doi.org/10.1021/acsami.6b12994>.
- [40] J. Teno, G. González-Gaitano, J. González-Benito, Poly(ethylene-co-vinyl acetate) films prepared by solution blow spinning: surface characterization and its relation with E. Coli adhesion, *Polym. Test.* 60 (2017) 140–148, <https://doi.org/10.1016/j.polymertesting.2017.03.020>.
- [41] A. Kasiri, J.E. Domínguez, J. González-Benito, Morphology optimization of solution blow spun polystyrene to obtain superhydrophobic materials with high ability of oil absorption, *Polym. Test.* 91 (2020), <https://doi.org/10.1016/j.polymertesting.2020.106859>.
- [42] J.E. Domínguez, A. Kasiri, J. González-Benito, Wettability behavior of solution blow spun polysulfone by controlling morphology, *J. Appl. Polym. Sci.* 138 (2021), <https://doi.org/10.1002/app.50200>.
- [43] G.C. Dadol, A. Kilić, L.D. Tijing, K.J.A. Lim, L.K. Cabatingan, N.P.B. Tan, E. Stojanovska, Y. Polat, Solution blow spinning (SBS) and SBS-spun nanofibers: materials, methods, and applications, *Mater. Today Commun.* 25 (2020) 101656, <https://doi.org/10.1016/j.mtcomm.2020.101656>.
- [44] M. Moradienayat, J. González-Benito, D. Olmos, Airbrushed PSF/ZnO composite coatings as a novel approach for the consolidation of historical bones, *Nanomaterials* 13 (2023), <https://doi.org/10.3390/nano13040625>.
- [45] J. González-Benito, D. Olmos, J. Teno, G. González-Gaitano, Nanomorphology and nanomechanical characteristics of solution-blow-spun PVDF-based fibers filled with carbon nanotubes, *J. Appl. Polym. Sci.* 136 (2019) 1–6, <https://doi.org/10.1002/app.47115>.
- [46] A. Kramar, T. Luxbacher, J. Gonzalez-Benito, Solution blow co-spinning of cellulose acetate with poly(ethylene oxide). Structure, morphology, and properties of nanofibers, *Carbohydr. Polym.* 320 (2023) 121225, <https://doi.org/10.1016/j.carbpol.2023.121225>.
- [47] J.E. Domínguez, E. Olivos, C. Vázquez, J.M. Rivera, R. Hernández-Cortes, J. González-Benito, Automated low-cost device to produce sub-micrometric polymer fibers based on blow spun method, *HardwareX* 10 (2021) e00218, <https://doi.org/10.1016/j.ohx.2021.e00218>.
- [48] J. González-Benito, J. Teno, G. González-Gaitano, S. Xu, M.Y. Chiang, PVDF/TiO₂ nanocomposites prepared by solution blow spinning: surface properties and their relation with S. Mutans adhesion, *Polym. Test.* 58 (2017) 21–30, <https://doi.org/10.1016/j.polymertesting.2016.12.005>.
- [49] J. González-Benito, D. Torres, C. Ballesteros, V.M. Ruiz, J. Teno, PVDF based nanocomposites produced by solution blow spinning, structure and morphology induced by the presence of MWCNT and their consequences on some properties, *Colloid Polym. Sci.* 297 (2019) 1105–1118, <https://doi.org/10.1007/s00396-019-04530-5>.
- [50] A.F. Stalder, G. Kulik, D. Sage, L. Barbieri, P. Hoffmann, A snake-based approach to accurate determination of both contact points and contact angles, *Colloids Surfaces A Physicochem. Eng. Asp.* 286 (2006) 92–103, <https://doi.org/10.1016/j.colsurfa.2006.03.008>.
- [51] A. Larrañaga, C. Bello-Álvarez, E. Lizundia, Cytotoxicity and inflammatory effects of chitin nanofibrils isolated from fungi, *Biomacromolecules* 24 (2023) 5737–5748, <https://doi.org/10.1021/acs.biomac.3c00710>.
- [52] L. Heux, J. Brugnerotto, J. Desbrières, M.-F. Versali, M. Rinaudo, Solid state NMR for determination of degree of acetylation of chitin and chitosan, *Biomacromolecules* 1 (2000) 746–751, <https://doi.org/10.1021/bm000070y>.
- [53] E. Lizundia, J.L. Vilas, L.M. León, Crystallization, structural relaxation and thermal degradation in poly(L-lactide)/cellulose nanocrystal renewable nanocomposites, *Carbohydr. Polym.* 123 (2015) 256–265, <https://doi.org/10.1016/j.carbpol.2015.01.054>.
- [54] E. Lizundia, D. Kundu, Advances in natural biopolymer-based electrolytes and separators for battery applications, *Adv. Funct. Mater.* 31 (2021) 2005646, <https://doi.org/10.1002/adfm.202005646>.
- [55] F. Wu, D. Feng, Y. Xie, D. Xie, Y. Mei, Role of phase compatibility in gas barrier improvement of biodegradable polymer blends for food packaging application, *Ind. Eng. Chem. Res.* 61 (2022) 5464–5474, <https://doi.org/10.1021/acs.iecr.1c04664>.
- [56] H.M. Shaikh, A. Anis, A.M. Poulouse, S.M. Al-Zahrani, N.A. Madhar, A. Alhamidi, S. H. Aldeligan, F.S. Alsubaie, Synthesis and characterization of cellulose triacetate obtained from date palm (*Phoenix dactylifera* L.) trunk mesh-derived cellulose, *Molecules* 27 (2022), <https://doi.org/10.3390/molecules27041434>.
- [57] S. Nam, A.D. French, B.D. Condon, M. Concha, Segal crystallinity index revisited by the simulation of X-ray diffraction patterns of cotton cellulose I β and cellulose II, *Carbohydr. Polym.* 135 (2016) 1–9, <https://doi.org/10.1016/j.carbpol.2015.08.035>.

- [58] X. Ju, M. Bowden, E.E. Brown, X. Zhang, An improved X-ray diffraction method for cellulose crystallinity measurement, *Carbohydr. Polym.* 123 (2015) 476–481, <https://doi.org/10.1016/j.carbpol.2014.12.071>.
- [59] D. Thi To Nu, N. Phi Hung, C. Van Hoang, B. Van der Bruggen, Preparation of an asymmetric membrane from sugarcane bagasse using DMSO as green solvent, *Appl. Sci.* 9 (2019), <https://doi.org/10.3390/app9163347>.
- [60] R.R.M. De Freitas, A.M. Senna, V.R. Botaro, Influence of degree of substitution on thermal dynamic mechanical and physicochemical properties of cellulose acetate, *Ind. Crop Prod.* 109 (2017) 452–458, <https://doi.org/10.1016/j.indcrop.2017.08.062>.
- [61] T.D. Nguyen, E. Sierra, H. Eguiraun, E. Lizundia, Iridescent cellulose nanocrystal films: the link between structural colour and Bragg's law, *Eur. J. Phys.* 39 (2018), <https://doi.org/10.1088/1361-6404/aab598>.
- [62] S. Park, J.O. Baker, M.E. Himmel, P.A. Parilla, D.K. Johnson, Cellulose crystallinity index: measurement techniques and their impact on interpreting cellulase performance, *Biotechnol. Biofuels* 3 (2010) 1–10, <https://doi.org/10.1186/1754-6834-3-10>.
- [63] F.N. Cobo, P.C.S. Faria-Tisher, J.L. Duarte, G.M. Carvalho, Preparation and characterization of microporous cellulose acetate films using breath figure method by spin coating technique, *Cellulose* 24 (2017) 4981–4995, <https://doi.org/10.1007/s10570-017-1459-7>.
- [64] L.C.M. Celuppi, A.P. Capelezzo, L.B. Cima, R.C.F. Zeferino, T.A. Carniel, M. Zanetti, J.M.M. de Mello, M.A. Fiori, H.G. Riella, Microbiological, thermal and mechanical performance of cellulose acetate films with geranyl acetate, *Int. J. Biol. Macromol.* 228 (2023) 517–527, <https://doi.org/10.1016/j.ijbiomac.2022.12.170>.
- [65] N.R.L. Pereira, B. Lopes, I.V. Fagundes, F.M. de Moraes, F.D.P. Morisso, G.O. C. Parma, K.M. Zepon, R.F. Magnago, Bio-packaging based on cellulose acetate from banana pseudostem and containing *Butia catarinensis* extracts, *Int. J. Biol. Macromol.* 194 (2022) 32–41, <https://doi.org/10.1016/j.ijbiomac.2021.11.179>.
- [66] A.A. Ibrahim, A.M. Adel, Z.H.A. El-Wahab, M.T. Al-Shemy, Utilization of carboxymethyl cellulose based on bean hulls as chelating agent. Synthesis, characterization and biological activity, *Carbohydr. Polym.* 83 (2011) 94–115, <https://doi.org/10.1016/j.carbpol.2010.07.026>.
- [67] L. Zhao, S. Lin, J. Lin, J. Wu, H. Chen, Effect of acid hydrolysis on the structural and antioxidant characteristics of β -glucan extracted from Qingke (Tibetan hullless barley), *Front. Nutr.* 9 (2022) 1–11, <https://doi.org/10.3389/fnut.2022.1052901>.
- [68] E. Lizundia, E. Fortunati, F. Dominici, J.L. Vilas, L.M. León, I. Armentano, L. Torre, J.M. Kenny, PLLA-grafted cellulose nanocrystals: role of the CNC content and grafting on the PLA bionanocomposite film properties, *Carbohydr. Polym.* 146 (2016) 105–113, <https://doi.org/10.1016/j.carbpol.2016.01.041>.
- [69] P.G. Gan, S.T. Sam, M.F. bin Abdullah, M.F. Omar, Thermal properties of nanocellulose-reinforced composites: a review, *J. Appl. Polym. Sci.* 137 (2020) 48544, <https://doi.org/10.1002/app.48544>.
- [70] R. Majumdar, U. Mishra, N. Mahata, M.P. Shah, A. Mondal, B. Bhunia, Preparation, characterization, and performance evaluation of composite films of polyvinyl alcohol/cellulose nanofiber extracted from *Imperata cylindrica*, *Chemosphere* 337 (2023) 139370, <https://doi.org/10.1016/j.chemosphere.2023.139370>.
- [71] R.L. Andersson, V. Ström, U.W. Gedde, P.E. Mallon, M.S. Hedenqvist, R.T. Olsson, Micromechanics of ultra-toughened electrospun PMMA/PEO fibres as revealed by in-situ tensile testing in an electron microscope, *Sci. Rep.* 3 (2014) 1–8, <https://doi.org/10.1038/srep06335>.
- [72] A. Li, Z. Han, Z. Li, J. Li, X. Li, Z. Zhang, A PTHrP-2 loaded adhesive cellulose acetate nanofiber mat as wound dressing accelerates wound healing, *Mater. Des.* 212 (2021) 110241, <https://doi.org/10.1016/j.matdes.2021.110241>.
- [73] S.C. Carroccio, P. Scarfato, E. Bruno, P. Aprea, N.T. Dintcheva, G. Filippone, Impact of nanoparticles on the environmental sustainability of polymer nanocomposites based on bioplastics or recycled plastics – a review of life-cycle assessment studies, *J. Clean. Prod.* 335 (2022) 130322, <https://doi.org/10.1016/j.jclepro.2021.130322>.
- [74] J. Turk, P. Oven, I. Poljanšek, A. Lešek, F. Knez, K. Malovrh Rebec, Evaluation of an environmental profile comparison for nanocellulose production and supply chain by applying different life cycle assessment methods, *J. Clean. Prod.* 247 (2020) 119107, <https://doi.org/10.1016/j.jclepro.2019.119107>.
- [75] X. Tian, J. Xie, M. Xu, Y. Wang, Y. Liu, An infinite life cycle assessment model to re-evaluate resource efficiency and environmental impacts of circular economy systems, *Waste Manag.* 145 (2022) 72–82, <https://doi.org/10.1016/j.wasman.2022.04.035>.
- [76] D.M. Maklavany, Z. Rouzitalab, M. Bazmi, M. Askarieh, A. Nabavi-Pelesaraei, Eco-environmental analysis of different routes for the synthesis of MIL-53(Fe): an integrated life cycle assessment and life cycle cost approaches, *ACS Sustain. Chem. Eng.* 11 (2023) 9816–9832, <https://doi.org/10.1021/acssuschemeng.3c02199>.